



Localization regime in diffusion NMR: Theory and experiments

Nicolas Moutal^{a,*}, Kerstin Demberg^{b,c}, Denis S. Grebenkov^a, Tristan Anselm Kuder^b

^aLaboratoire de Physique de la Matière Condensée, Ecole Polytechnique, CNRS, IP Paris, 91128 Palaiseau, France

^bMedical Physics in Radiology, German Cancer Research Center (DKFZ), Heidelberg, Germany

^cFaculty of Physics and Astronomy, Heidelberg University, Heidelberg, Germany

ARTICLE INFO

Article history:

Received 24 April 2019

Revised 27 June 2019

Accepted 28 June 2019

Available online 2 July 2019

Keywords:

Localization regime

High gradients

PGSE

ABSTRACT

In this work we investigate the emergence of the localization regime for diffusion NMR in various geometries: inside slabs, inside cylinders and outside rods arranged on a square array. At high gradients, the transverse magnetization is strongly attenuated in the bulk, whereas the macroscopic signal is formed by the remaining magnetization localized near boundaries of the sample. As a consequence, the signal is particularly sensitive to the microstructure. The theoretical analysis relies on recent mathematical advances on the study of the Bloch-Torrey equation. Experiments were conducted with hyperpolarized xenon-129 gas in 3D-printed phantoms and show an excellent agreement with numerical simulations and theoretical predictions. Our mathematical arguments and experimental evidence indicate that the localization regime with a stretched-exponential decay of the macroscopic signal is a generic feature of diffusion NMR that can be observed at moderately high gradients in most NMR scanners.

© 2019 Elsevier Inc. All rights reserved.

1. Introduction

Diffusion magnetic resonance imaging (dMRI) is a non-invasive technique which aims at unraveling the microstructural properties of a sample through the measurement of diffusion of spin-bearing nuclei (e.g., protons in water molecules) [1–3]. One may probe finer-scale details by increasing the magnetic field gradient g or the b -value ($b \propto g^2$, see below), which characterizes the strength of the diffusion encoding. For example, very large b -values, up to $100 \text{ ms}/\mu\text{m}^2$, were employed for investigating the rat brain [4] and for reconstructing neuronal fiber pathways in the human brain [5]. In contrast, many theoretical approaches rely on small b approximations. In fact, the assumption of small b -values allows one to expand the dMRI signal in powers of b (cumulant expansion) and truncate it to its first terms [3,6,7]. In particular, the first term of the cumulant expansion yields the classical Gaussian phase approximation for the signal $E = e^{-bD}$, where D is the effective (or apparent) diffusion coefficient of spin-bearing particles in the sample that may differ from their intrinsic diffusion coefficient D_0 .

The range of validity of the cumulant expansion and related approximations was first studied theoretically by Stoller et al. [8], who showed that the cumulant expansion has a finite convergence radius and that a new regime emerges at higher gradients.

This so-called “localization regime” [9] was observed experimentally by Hürlimann et al. for water in slabs of width $160 \mu\text{m}$ at gradients as small as 20 mT/m and b -values of about $10 \text{ ms}/\mu\text{m}^2$ [10]. It features a very strong deviation from the Gaussian phase approximation (and more generally from cumulant expansion approximations) for the signal, with $-\ln(E) \propto (bD_0)^{1/3}$. Moreover, due to the high b -values the transverse magnetization far from the boundaries of the medium vanishes and only a thin layer of thickness $\ell_g = (D_0/G)^{1/3}$ near the boundaries contributes to the measured signal (with $G = \gamma g$, where γ is the gyromagnetic ratio of the diffusing nuclei). Here, ℓ_g denotes the gradient length, which can be interpreted as the typical diffusion length traveled by nuclei during the time needed to reach uncorrelated phases. This feature makes the signal at high b -values particularly sensitive to the microstructure [11]. The influence of the permeability of the boundaries was studied in [12,13] and it was shown that the localization of the magnetization near the boundaries enhances the dependence of the resulting signal on the permeability. The localization regime was shown to emerge when the gradient length ℓ_g is much smaller than (i) the diffusion length traveled by spins during the gradient sequence and (ii) the typical size of confining domains (e.g., width of the slab, in the experiment by Hürlimann et al).

To our knowledge, the work by Hürlimann et al. [10] on diffusion in a slab is the only undeniable experimental evidence of the localization regime. While deviations from the Gaussian phase approximation were abundantly observed in biological tissues and mineral samples [6,14–22], it is usually difficult to identify

* Corresponding author.

E-mail addresses: nicolas.moutal@polytechnique.edu (N. Moutal), denis.grebenkov@polytechnique.edu (D.S. Grebenkov).

unambiguously the origin of these deviations. In other words, the observed deviations may be related to the localization regime, but may also originate from co-existing populations of water with different effective diffusion coefficients, mixture of restricted and hindered diffusion, etc. The existence of the localization regime in more general domains and, in particular, in unbounded domains (e.g., the extracellular space) has not yet been addressed experimentally. In this paper, we present experimental data, numerical simulations and theoretical arguments showing the emergence of the localization regime in two complementary geometries: diffusion inside cylinders and diffusion outside an array of rods. We also treat a slab geometry as a reference case.

The paper is organized as follows. First, we present in Section 2 the theoretical ground that we use to interpret the experimental results. Section 3 describes the experimental setup and the numerical simulations. In Section 4, we show that our theoretical analysis and numerical computations are in excellent agreement with the experimental data. The characteristic stretched-exponential decay of the signal in the localization regime is observed at moderately high gradients and in various geometries, including unbounded diffusion outside obstacles. We discuss the implications of these results and conclude the paper in Section 5. Appendix A brings additional insights onto the localization regime with curved boundaries and Appendix B provides some clarification about the mathematical definition of the spectrum of a differential operator.

2. Theory

The evolution of the transverse magnetization M in the simplest case of a constant magnetic field gradient g is described by the Bloch-Torrey equation [23]:

$$\frac{\partial M}{\partial t} = (D_0 \nabla^2 - iGx)M, \quad (1)$$

where we chose the x -axis as the gradient direction. Throughout the paper, we use the notation $G = \gamma g$. The differential operator on the right-hand side of the equation, $D_0 \nabla^2 - iGx$, that we call the “Bloch-Torrey operator” in the following, can be treated as a perturbation of the classical diffusion (or Laplace) operator $D_0 \nabla^2$, in the regime of small gradients. However, the iGx term makes the whole operator non-Hermitian, which affects deeply its spectral properties [8,13,24,25]: its spectrum may become discrete or even empty in unbounded domains (see Appendix B); the eigenvalues are complex; the eigenmodes are no longer orthogonal to each other (in the Hermitian sense) and they do not necessarily form a complete basis [26,27]. These mathematical facts illustrate that theoretical approaches where the gradient term is treated as a small perturbation may be insufficient to fully understand the signal formation.

In the following, we analyze the behavior of the transverse magnetization, hence the signal, at high gradients and relatively long encoding times, which are the conditions of emergence of the localization regime. This section summarizes and further extends the theoretical ground developed in [3,8–12,28]. Throughout this paper, we focus on the Bloch-Torrey Eq. (1) with the linear gradient, although similar features may be relevant to other spatial profiles of the magnetic field, e.g. the dipole field (see [29,30] and references therein).

2.1. Eigenmode decomposition

We first consider a spin echo sequence with constant gradient g , where the duration of the gradient before and after the refocusing pulse is δ . Later, the more general case with a finite gap $\Delta - \delta$ between the two gradient pulses is considered (where Δ is the separation between the start of the two encoding pulses).

In bounded domains, the term iGx is bounded and one can show that the complex-valued eigenmodes v_n of the Bloch-Torrey operator form a complete basis, except at some exceptional values of G (that we neglect in the following, see [24]). These eigenmodes and the corresponding eigenvalues depend on G . Since the Bloch-Torrey operator is symmetric, the eigenmodes are “rectanormal” [8] in the sense that, after appropriate normalization, they satisfy the following orthogonality relation (not to be confused with the Hermitian orthogonality relation, in which $v_m(\mathbf{r})$ is replaced by its complex conjugate $v_m^*(\mathbf{r})$):

$$\int_{\Omega} v_n(\mathbf{r}) v_m(\mathbf{r}) d\mathbf{r} = \begin{cases} 0 & \text{if } n \neq m \\ 1 & \text{if } n = m \end{cases} \quad (2)$$

This allows one to project functions onto the $\{v_n\}_{n \geq 1}$ basis by using standard formulas. Let us assume that the initial condition is a uniform magnetization after the exciting 90° radio frequency (RF) pulse, i.e. $M(\mathbf{r}, t = 0) = 1/V$, where V is the volume of the domain Ω . Hence we decompose the transverse magnetization as:

$$M(\mathbf{r}, t) = \frac{1}{\sqrt{V}} \sum_{n \geq 1} \mu_n v_n(\mathbf{r}) e^{-\lambda_n t}, \quad (3)$$

where μ_n are complex coefficients given by

$$\mu_n = \frac{1}{\sqrt{V}} \int_{\Omega} v_n(\mathbf{r}) d\mathbf{r}, \quad (4)$$

and λ_n are the corresponding eigenvalues:

$$-(D_0 \nabla^2 - iGx) v_n = \lambda_n v_n. \quad (5)$$

We set the minus sign in front of the Bloch-Torrey operator to have eigenvalues with a positive real part, thus we sort λ_n by increasing real part. Note that the normalization of μ_n by $1/\sqrt{V}$ makes it dimensionless.

At the end of the first gradient pulse (i.e., at $t = \delta$), a refocusing 180° RF pulse is applied, which is equivalent to applying a complex conjugation to the magnetization M :

$$\begin{aligned} M(\mathbf{r}, \delta + 0) &= \frac{1}{\sqrt{V}} \sum_{n \geq 1} \mu_n^* v_n^*(\mathbf{r}) e^{-\lambda_n^* \delta} \\ &= \frac{1}{\sqrt{V}} \sum_{n \geq 1} \mu_n^* e^{-\lambda_n^* \delta} \sum_{m \geq 1} \beta_{n,m} v_m(\mathbf{r}), \end{aligned} \quad (6)$$

where we have decomposed each v_n^* over the eigenmode basis $(v_m)_{m \geq 1}$, with complex coefficients $\beta_{n,m}$:

$$\beta_{n,m} = \int_{\Omega} v_n^*(\mathbf{r}) v_m(\mathbf{r}) d\mathbf{r}.$$

Finally, after the second gradient pulse, the transverse magnetization is equal to

$$M(\mathbf{r}, 2\delta) = \frac{1}{\sqrt{V}} \sum_{n,m \geq 1} \mu_n^* \beta_{n,m} v_m(\mathbf{r}) e^{-(\lambda_n^* + \lambda_m) \delta}, \quad (8)$$

and the signal can be computed from

$$E = \int_{\Omega} M(\mathbf{r}, 2\delta) d\mathbf{r} = \sum_{n,m \geq 1} \mu_n^* \beta_{n,m} \mu_m e^{-(\lambda_n^* + \lambda_m) \delta}. \quad (9)$$

Although the transverse magnetization (8) is complex, the resulting macroscopic signal (9) is real.

2.2. Localization regime and gradient length

In the regime of long encoding times δ , one can truncate the above decompositions to their first terms:

$$M(\mathbf{r}, 2\delta) \approx \frac{1}{\sqrt{V}} \mu_1^* \beta_{1,1} v_1(\mathbf{r}) e^{-2\text{Re}(\lambda_1)\delta}, \quad (10)$$

$$E \approx C_{1,1} e^{-2\text{Re}(\lambda_1)\delta}, \quad (11)$$

where the coefficient $C_{1,1} = |\mu_1^* \beta_{1,1}|$ typically decreases slowly with G as compared to the exponential factor. This approximation is valid if the next-order terms are negligible. This may happen if the next eigenvalue is sufficiently far from λ_1 , i.e., $|e^{-\lambda_2\delta}| \ll |e^{-\lambda_1\delta}|$, or if the weights $\mu_n^* \beta_{n,m}$ and $\mu_n^* \beta_{n,m} \mu_m$ (with $(n, m) \neq (1, 1)$) are small enough. Note that the eigenvalues may come in complex conjugated pairs, in which case the above expressions (10) and (11) would involve four terms (two diagonal terms and two cross terms) with similar exponential decays $e^{-2\text{Re}(\lambda_i)\delta}$. We show in Section 2.3 that these additional terms may produce oscillations in the signal on top of the overall decay (11). For clarity, we first focus on Eq. (11) in this subsection.

In this regime, the behavior of the magnetization, and thus the signal, is dictated by the dependence of $\text{Re}(\lambda_1)$ on the gradient G . In [8,9,12,13,24], an asymptotic expansion for the λ_n at high gradients was derived. In particular, the first term of the expansion of the first eigenvalue is universal:

$$2\text{Re}(\lambda_1) = |a'_1| \frac{D_0}{\ell_g^2} + O(\ell_g^{-3/2}) \quad (g \rightarrow \infty), \quad (12)$$

where $\ell_g = (D_0/G)^{1/3}$ is the gradient length and $a'_1 \approx -1.02$ is the first zero of the derivative of the Airy function $\text{Ai}(z)$. This formula is universal in the sense that it does not depend on the geometry of the domain: in fact, any smooth boundary looks as a flat surface when probed at a length scale $\ell_g \rightarrow 0$. In turn, Eq. (12) is exact without any correction terms for a flat boundary. By combining Eqs. (10) and (12), one gets the stretched-exponential behavior, which is a hallmark of the localization regime,

$$-\ln(E) \propto (\ell_\delta/\ell_g)^2 \propto (bD_0)^{1/3} \quad (bD_0 \gg 1), \quad (13)$$

where $\ell_\delta = \sqrt{D_0\delta}$ is the diffusion length during the gradient pulse, and $b = 2G^2\delta^3/3$ for this gradient profile.

In order to offer an interpretation for the gradient length ℓ_g , let us consider several nuclei that start at the same position and diffuse freely (i.e., they do not encounter any boundary or obstacle) under the magnetic field gradient g . After a time t , the nuclei are typically spread over a distance of the order of $\sqrt{D_0 t}$, and thus have accumulated a random phase difference of the order of $Gt\sqrt{D_0 t}$. The nuclei have practically uncorrelated phases when this difference is comparable with 2π , which yields a decorrelation time: $t_g = (G^2 D_0)^{-1/3}$. Note that by time-reversal, t_g can also be interpreted as the time beyond which several diffusing particles arriving at the same position have almost uncorrelated phases. The gradient length ℓ_g is then the typical distance traveled by these particles during time t_g : $\ell_g = \sqrt{D_0 t_g}$.

If the gradient length ℓ_g is much smaller than the typical size of the medium ℓ_s and the diffusion length ℓ_δ , then nuclei at any point not too close to a boundary have completely uncorrelated phases and the resulting magnetization is negligible. As the motion of the nuclei is restricted near the boundary, the remaining magnetization at the echo time is localized in a thin layer of thickness ℓ_g close to the boundary: this is the localization regime. In regard to Eq. (10), the localization regime corresponds to the localization of the first eigenmodes of the Bloch-Torrey operator at high gradients over a width ℓ_g [11,12,24]. This localization occurs where the gradient is orthogonal to the boundary, i.e. where the boundary prevents diffusion along the gradient direction the most.

2.3. Dependence on the geometry

Although the first term of the high-gradient expansion (12) of the eigenvalues of the Bloch-Torrey operator is universal, the next-order terms depend on the geometry of the domain, and more precisely on the curvature, permeability, and surface relaxivity of the boundary at the points where the localization occurs [12,13,24]. Throughout the article, we discard permeability and surface relaxivity and consider only the effect of curvature. In two dimensions, if one denotes by R_c the curvature radius at a localization point, then the eigenvalues associated to the eigenmodes localized near that point can be expanded as [24]

$$2\text{Re}(\lambda_{k,l}) = |a'_k| \frac{D_0}{\ell_g^2} + (2l-1) \frac{D_0}{|R_c|^{1/2} \ell_g^{3/2}} - \frac{\sqrt{3} D_0}{2|a'_k| R_c \ell_g} + O(\ell_g^{-1/2}), \quad (14)$$

where a'_k is the k -th zero of the derivative of the Airy function, and the indices k, l are positive integers (the eigenvalue with the smallest real part is given by $k = l = 1$). As we explain in Appendix A, Eq. (14) extends to three-dimensional domains as

$$2\text{Re}(\lambda_{k,l_1,l_2}) = |a'_k| \frac{D_0}{\ell_g^2} + \frac{D_0}{\ell_g^3} \left(\frac{2l_1-1}{|R_{c,1}|^{1/2}} + \frac{2l_2-1}{|R_{c,2}|^{1/2}} \right) - \frac{\sqrt{3} D_0}{2|a'_k| \ell_g} \left(\frac{1}{R_{c,1}} + \frac{1}{R_{c,2}} \right) + O(\ell_g^{-1/2}), \quad (15)$$

where $R_{c,1}$ and $R_{c,2}$ are the principal radii of curvature of the boundary at the localization point and k, l_1, l_2 are positive integers. For cylinders and parallel circular rods, one radius of curvature is infinite, and Eq. (15) is reduced to Eq. (14), reflecting effectively the two-dimensional character of diffusion in these geometric settings. In the following we focus on the formula (14) for two-dimensional geometries, which corresponds to our experimental setup (see Section 3). In the third term of Eq. (14) the sign of the curvature radius R_c should be taken into account: positive for a concave boundary (e.g., interior of a cylinder) and negative for a convex boundary (e.g., exterior of a cylinder).

As we discuss in Appendix A, the first term of expansion (14) is related to the variation of the eigenmode along the gradient direction and the second term is related to the variation of the eigenmode along the boundary. These terms are associated with different length scales that correspond to the localization along the gradient, ℓ_g , and to the localization parallel to the curved boundary, $\ell_{g,\parallel} = (2|R_c| \ell_g^3)^{1/4}$. As a consequence, localization along the gradient and along the boundary develops at different time scales defined by the conditions $\ell_\delta \gg \ell_g$ and $\ell_\delta \gg \ell_{g,\parallel}$ (see Fig. A.11 in Appendix A). Note that localization typically occurs under the additional condition $\ell_g \ll |R_c|$ so that $\ell_g < \ell_{g,\parallel}$. When $|R_c| \rightarrow \infty$, the spectrum becomes denser and denser due to the contribution from the lateral modes, and we show in Appendix A that one may sum the lateral eigenmodes and recover the magnetization for a flat boundary.

Another effect of the geometry is the overlapping of localization pockets. In fact, to each localization point (at which the gradient is perpendicular to the boundary) is associated a family of eigenmodes and eigenvalues described by Eq. (14) at high gradient. As a consequence, the smallest eigenvalues from different families can contribute to the signal even at large δ , whereas the overlap between corresponding eigenmodes may lead to oscillating patterns.

To illustrate this effect, let us consider the simple example of a slab of width L (with the gradient direction being orthogonal to the slab). Note that this geometry is reduced to a one-dimensional interval $[-L/2, L/2]$ of length L . In this setting, the eigenmodes of the Bloch-Torrey operator can be localized at either of two

endpoints of the interval, but only if the gradient length ℓ_g is much smaller than L . In fact, as we stated in Section 2.2, ℓ_g represents approximately the width of the localized eigenmodes. For example, Stoller et al. computed that the first eigenmodes start to localize at each side of the slab when $\ell_g < 0.38L$. Due to the left-right symmetry ($x \rightarrow -x$), the first two eigenmodes $v_1(x)$ and $v_2(x)$ satisfy the identity $v_2(x) = v_1^*(-x)$ and $\lambda_2 = \lambda_1^*$, and are localized at each endpoint of the interval. Thus the first two eigenvalues have the same real part and, in the limit of large δ , the magnetization may be represented by a superposition of v_1 and v_2 :

$$M(x, 2\delta) \approx (c_{1,1} + c_{2,1}e^{-2i\text{Im}(\lambda_1)\delta})e^{-2\text{Re}(\lambda_1)\delta}v_1(x) + (c_{2,2} + c_{1,2}e^{2i\text{Im}(\lambda_1)\delta})e^{-2\text{Re}(\lambda_1)\delta}v_2(x), \quad (16)$$

with $c_{n,m} = \mu_n^* \beta_{n,m} / \sqrt{V}$, and the signal is given by

$$E \approx Ce^{-2\text{Re}(\lambda_1)\delta}, \quad (17)$$

with

$$C = 2(C_{1,1} + \text{Re}(C_{1,2})), \quad (18)$$

where $C_{1,1}$ was previously introduced in Eq. (11) and $C_{1,2}$ is an oscillating function of g and δ given by

$$C_{1,2} = \mu_1^* \beta_{1,2} \mu_2 e^{2i\text{Im}(\lambda_1)\delta}. \quad (19)$$

The factor 2 in (18) reflects the fact that two eigenmodes contribute to the signal. For a slab, one can compute the following expansion for the imaginary part of the first eigenvalue [8]:

$$2\text{Im}(\lambda_1) = \pm \left(GL - \sqrt{3} |a_1| \frac{D_0}{\ell_g^2} \right) + O(\ell_g^{-3/2}), \quad (20)$$

where the \pm sign is merely a matter of convention (given that $\lambda_2 = \lambda_1^*$). Since at high gradients the imaginary part of λ_1 scales as G and its real part scales as $G^{2/3}$, the oscillations in the signal are somewhat faster than its global decay. In other words, the signal may exhibit several oscillations before reaching the noise floor. One may note that the dominant term, GL , of the imaginary part depends on the choice of origin $x = 0$. However, Eq. (19) was derived under the assumption of a symmetric slab, i.e. $x = 0$ at the middle of the slab. In the general case, the imaginary parts of the eigenvalues enter through their differences in the expression of the signal, thus the arbitrary choice of the origin $x = 0$ has no influence on the expression of the signal, as it should be for a refocused gradient sequence. Note that the eigenmodes of the Bloch-Torrey operator in a slab are known explicitly and can be written in terms of Airy functions, see [8,12,13].

The conclusion of this computation is that the cross-term $C_{1,2}$ produces oscillations in the signal (by varying g or δ) on top of the asymptotic decay (11). The definition (7) of $\beta_{n,m}$ implies that this cross-term is linked to the overlapping of the modes v_1 and v_2 . In turn, this overlapping depends on the ratio between the width ℓ_g of the modes, and their spacing L : the smaller the ratio ℓ_g/L , the smaller the overlapping, and thus, the smaller the oscillating term. In the limit of well-separated modes, $\beta_{1,2} = 0$ and one has $C = 2C_{1,1}$. The effect of overlapping of eigenmodes is illustrated in Fig. 1 where we plotted the transverse magnetization in a slab for two different gradient strengths: at low gradients the localization pockets overlap and at high gradients they are well-separated. Note that we plotted only the real part of the magnetization; the imaginary part is non-zero but it does not contribute to the signal since its integral over the slab is zero. Although we illustrated this overlapping effect on the simple example of a slab, the conclusion (and the previous computations) may be generalized to any geom-

etry, where L would denote the spacing between two localized eigenmodes.

2.4. The influence of $\Delta - \delta$

Until now we have considered a PGSE sequence with $\Delta = \delta$, i.e. without any gap between two gradient pulses. In this section we consider a more general PGSE sequence and investigate the influence of the diffusion step duration $\Delta - \delta$ on the transverse magnetization. Mathematically, the effect of this diffusion step is to multiply the transverse magnetization just after the first gradient pulse by the operator $\mathcal{D} = \exp((\Delta - \delta)D_0\nabla^2)$. Then Eqs. (8), (9), and the consequent analysis remain applicable with the new definition for the coefficients $\beta_{n,m}$:

$$\beta_{n,m} = \int_{\Omega} (\mathcal{D}v_n^*)(\mathbf{r})v_m(\mathbf{r})d\mathbf{r}. \quad (21)$$

The dependence on $\Delta - \delta$ is now hidden in the coefficients $\beta_{n,m}$. Note that if $\Delta = \delta$, then the operator \mathcal{D} is the identity (since diffusion during zero time does not affect the magnetization) and we recover the previous definition (7) for $\beta_{n,m}$. If we consider the regime of long δ where only the first eigenmode contributes, Eq. (8) is reduced to Eq. (10) and thus the effect of the diffusion step results merely in a modification of the global amplitude of the magnetization through the new definition (21) of the coefficient $\beta_{1,1}$. In turn, the global amplitude of the signal in Eq. (11) is also affected by this coefficient and decreases with increasing $\Delta - \delta$.

The situation of two overlapping eigenmodes is more complex. The diffusion step also changes the values of the coefficients $\beta_{1,2}$, $\beta_{2,1}$, and hence the relative amplitude of the oscillating term $C_{1,2}$ (see Eqs. (18) and (19)). Diffusion is expected to increase the width of the localized eigenmodes, thus increasing the overlapping between them and enhancing the oscillations in the signal. This effect should be stronger for already overlapping modes than for well separated ones, in other words, when the ratio ℓ_g/L is not very small, where L denotes the distance between two localization pockets. The effect of the diffusion step on the localization regime in a one-dimensional setting was partly investigated in [12].

2.5. Unbounded domains

In the previous subsections, we assumed that diffusion takes place in a bounded domain Ω , and this hypothesis ensured the validity of the decomposition of the transverse magnetization over the Bloch-Torrey eigenmodes basis (3). However, this assumption excludes some physically relevant cases, such as extracellular diffusion, which are described by unbounded domains. In this section, we discuss few known mathematical properties and the applicability of the previous results to such domains.

The most striking property of the Bloch-Torrey operator is that, in most unbounded domains, its spectrum is discrete [25], even though the spectrum of the Laplacian operator ∇^2 is continuous. In other words, the iGx term, which is responsible for the discreteness of the spectrum, cannot be considered as a small perturbation of the diffusion operator $D_0\nabla^2$. However, there is no rigorous mathematical proof that the eigenmodes form a complete basis in such domains. We conjecture that this property still holds except for trivial cases (such as free space, which leads to an empty spectrum). In [24], a construction of approximate eigenmodes and eigenvalues was performed and Eqs. (14) and (20) are valid for unbounded domains as well.

Despite its practical importance, few theoretical studies addressed the range of validity of the Gaussian phase approximation (and more generally the cumulant expansion) in unbounded domains [11]. In the following sections, we investigate

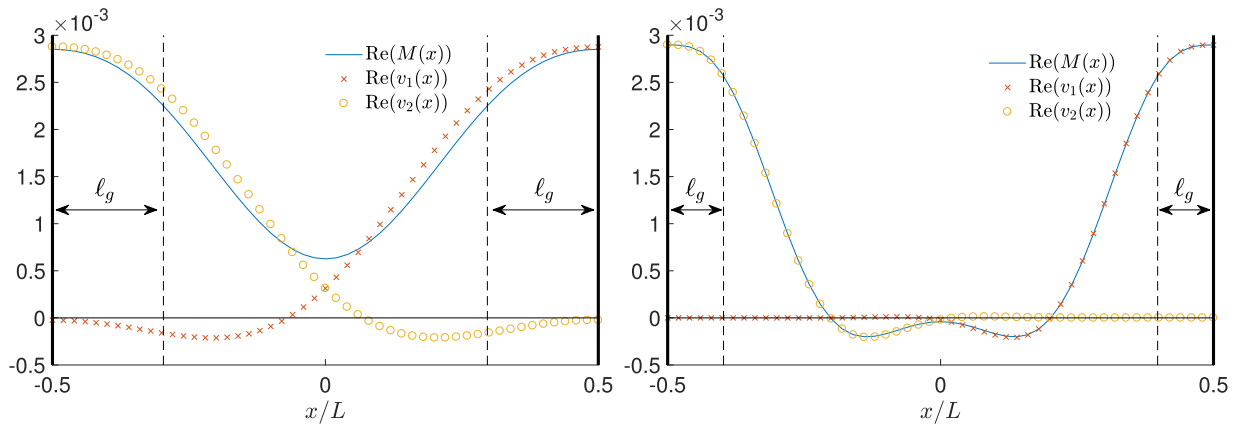


Fig. 1. The real part of the transverse magnetization $M(x)$ in a slab for two different gradient strengths, in the long δ regime, as well as the real part of the first two eigenmodes $v_1(x)$ and $v_2(x)$ weighted by the coefficients in front of $v_1(x)$ and $v_2(x)$ in Eq. (16). We checked that Eq. (16), i.e. the superposition of $v_1(x)$ and $v_2(x)$, reproduces perfectly the exact magnetization $M(x)$ in this regime. The computations were performed with a matrix formalism (described in Section 3). In both cases, one observes the localization of the magnetization near the endpoints of the interval. We chose a constant ratio $\ell_g/\ell_g = 2.5$ for both figures, so that the amplitude of the magnetization is approximately the same (see Eq. (13)). (left) $\ell_g/L \approx 0.2$: one can see some overlapping between the two eigenmodes and $|\beta_{1,2}| = 0.23$. (right) $\ell_g/L \approx 0.1$: there is almost no overlapping of the eigenmodes and $|\beta_{1,2}| = 8.2 \cdot 10^{-4}$.

experimentally the emergence of the localization regime in such a domain (array of rods).

3. Material and methods

Experiments were performed using hyperpolarized xenon-129 gas ($\gamma \approx 74 \cdot 10^6 \text{ s}^{-1}\text{T}^{-1}$) continuously flowing through phantoms containing different diffusion barrier geometries. Utilizing gas diffusion compared to water diffusion entails a several orders of magnitude larger diffusion coefficient which allows probing structures on the millimeter scale, which can easily be constructed with 3D-printers. Due to the weak signal of thermally polarized gas, hyperpolarized xenon gas with a considerably higher NMR signal was employed. Hyperpolarization was achieved by Rb/Xe-129 spin-exchange optical pumping (SEOP) [31–33]. For technical reasons [31], a gas mixture (Air Liquide Deutschland GmbH, Düsseldorf, Germany) composed of xenon (0.95 Vol%), nitrogen (8.75 Vol%) and helium-4 (rest) was used. The free diffusion coefficient of xenon in this gas mixture was measured to be $D_0 = (3.7 \pm 0.2) \cdot 10^{-5} \text{ m}^2\text{s}^{-1}$ [34], which is one order of magnitude larger than for pure xenon gas [35]. The gas was transferred at a small constant flow (approximately 150 mL/min) to the phantom positioned in an in-house built xenon coil in the isocenter of the magnet of a 1.5 T clinical MR scanner (Magnetom Symphony, A Tim System, Siemens Healthcare, Erlangen, Germany) with a maximal employed gradient amplitude of 32 mT/m. The experimental set-up and hyperpolarization process are detailed in [34,36].

The phantoms used are illustrated in Fig. 2 and described in Table 1. Phantom 1 contains parallel plates separated by a distance of $L = 3 \text{ mm}$, built by the in-house workshop from PMMA. For the phantoms 2 and 3, two blocks containing cylindrical tubes (with two different diameters $2R$) in a hexagonal arrangement were 3D-printed. Here, the gas diffuses inside the cylinders. Since all cylinders are identical and isolated from each other, this setting is equivalent to a single cylinder of diameter $2R$. Phantoms 4 and 5 consist of cylindrical solid rods on a square grid attached to a base plate and a roof plate with holes for gas in and out flow, so that the gas diffuses outside the cylinders. The geometry is defined by the diameter of the rods ($2R$) and by the rod center-to-center distance (L).

Phantoms 2–5 were printed with the PolyJet technology (Objet30 Pro, VeroClear as printing material, Stratasys, Ltd., Eden

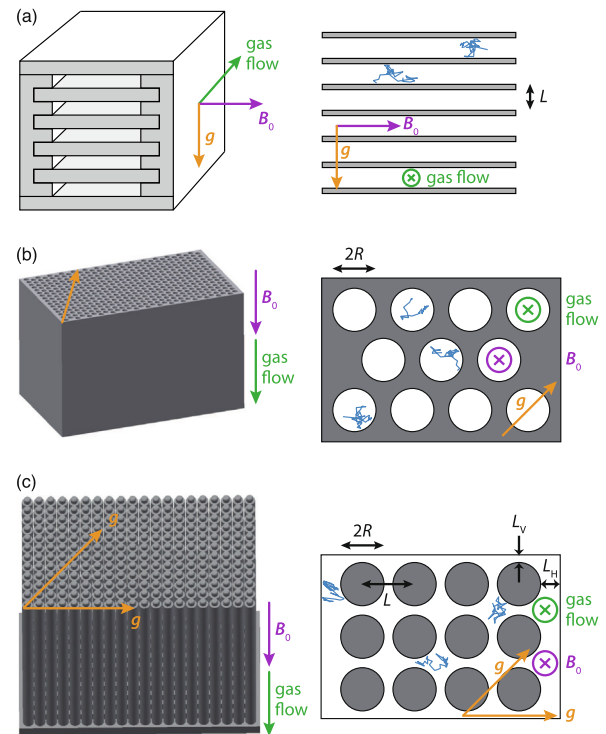


Fig. 2. Phantoms with corresponding magnified schematic depiction showing relevant length scales. (a) Phantom 1: Parallel plates. (b) Phantoms 2 and 3: Cylindrical tubes. (c) Phantoms 4 and 5: Cylindrical rods on a square grid.

Table 1
Characteristics of the phantoms (see Fig. 2).

#	Geometry	Dimensions
1	Slab	$L = 3 \text{ mm}$
2	Cylinders	$2R = 3.8 \text{ mm}$
3	Cylinders	$2R = 2 \text{ mm}$
4	Array of rods	17×10 rods $2R = 3.2 \text{ mm}; L = 4 \text{ mm}$ $L_V = 1.48 \text{ mm}; L_H = 1.35 \text{ mm}$
5	Array of rods	20×10 rods $2R = 3.2 \text{ mm}; L = 3.4 \text{ mm}$ $L_V = 0.78 \text{ mm}; L_H = 1.08 \text{ mm}$

Prairie, MN, USA) and then inserted in a casing with a base area of 70.1 mm × 42.3 mm. Consequently, for phantoms 4 and 5, there are border regions between the array of rods and the enclosing walls in which diffusion also takes place. For all phantoms, surface relaxivity and permeation can be ignored for high-gradient experiments.

Phantom 1 was positioned with the gas flow directed in the horizontal direction perpendicular to the main magnetic field and the gradient vector was pointing in the vertical direction in a sagittal slice of 50 mm thickness orthogonal to the plates and to the gas flow direction, see Fig. 2. Phantoms 2–5 were positioned with the gas flow directed parallel to the main magnetic field and the gradients were applied in the transversal plane of the scanner orthogonal to the gas flow direction (slice thickness 45 mm). For phantoms 4 and 5, measurements were taken with the gradient vector pointing along the left-right direction or the diagonal direction. In all cases, the gas flow did not influence the diffusion-weighted NMR signal.

A pulsed-gradient spin-echo (PGSE) sequence was applied as depicted in Fig. 3. The durations δ of the trapezoidal gradient pulses were set to 6 ms and include flat top time plus the ramp-up time of $\epsilon = 0.32$ ms. The gradient separation time was $\Delta = 9.34$ ms. The diffusion-weighted signal was sampled by gradually increasing the gradient amplitude in 32 steps from 0 to $g_{\max} = 32$ mT/m, recording the spin echo signal and acquiring up to 15 averages. The time between two consecutive 90° excitation pulses, i.e. the time between two measurements, was set to 18 s to restore the polarization in the phantom via gas flow. To account for fluctuations in the polarization level the recorded spin echo was averaged and normalized to an additional signal pre-readout directly after the 90° excitation pulse. To obtain the diffusion-induced signal attenuation, all points were normalized to the point acquired without diffusion weighting (i.e., at $g = 0$). The SNR at low gradient strength was in the order of 1000.

The numerical computation of the signal in a slab and in a cylinder is effectively reduced to that in an interval and a disk, respectively. For these simple shapes, the most efficient and accurate computation of the signal is realized with the matrix formalism [3,37–39], in which the Bloch-Torrey equation is projected onto the basis of explicitly known Laplacian eigenmodes to represent the signal via matrix products and exponentials (see [40,41] for details). The matrix formalism was also used to compute the transverse magnetization in these two domains (see similar computations in [12]). In turn, the numerical computation of the signals for phantoms 4 and 5 (arrays of rods) was performed differently. While the matrix formalism could in principle be applied, the need for a numerical computation of Laplacian eigenmodes in such structures makes this approach less efficient. Thus, we performed Monte Carlo simulations including the borders around the rod arrays with $2.5 \cdot 10^7$ random walkers and $1.6 \cdot 10^5$ steps per random walk trajectory. In order to compute the eigenmodes of the Bloch-Torrey operator in the rods geometry, we used the PDE solver from Matlab (The MathWorks, Natick, MA USA) in a square array of 3×3 rods with Dirichlet boundary conditions on the outer boundary and we kept only the eigenmodes that were localized on the central rod. Since the distance from the central rod to the outer boundary is about L , which was much larger than l_g and l_δ in our simulations, the effect of the outer boundary is negligible, so that the computed eigenmodes are very close to the ones for the infinitely periodic array of rods.

4. Results

We present the experimental and numerical results for diffusion in three different geometries: inside slabs, inside cylinders,

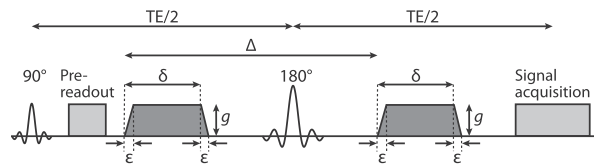


Fig. 3. PGSE sequence. The spin echo forms at time TE.

and outside arrays of rods. The localization regime in the slab geometry was already investigated experimentally by Hürlimann et al. [10], whereas only a few theoretical studies were devoted to the cylinder geometry [9,11,24]. The signal for an array of rods was previously computed numerically in [11] using a finite-element method [42].

For our particular gradient sequence and the parameters of the xenon gas mixture, one can compute $l_\delta = 0.5$ mm and l_g decreases from 0.8 mm to 0.25 mm for g ranging from 1 mT/m to 32 mT/m. So, by increasing the gradient, l_g crosses l_δ and the localization regime emerges.

4.1. Slab geometry

We choose the axes such that the slab is orthogonal to the z -axis. Note that this convention is different from the one that we adopted in Section 2, where the gradient was directed along the x -axis. One can then decompose the diffusive motion independently along the three axes x , y , z and get

$$E = \exp(-bD_0 \sin^2 \theta) E_{\text{slab}}(L, g \cos \theta), \quad (22)$$

where θ is the angle between the gradient and the z -axis and $E_{\text{slab}}(L, g)$ is the signal from an interval of length L . Here, the first factor is the signal attenuation due to diffusion in the lateral plane xy , which is almost free as outer boundaries are separated by distances that greatly exceed both l_g and l_δ (about 40 mm). One gets the slowest decay by ensuring that the gradient is orthogonal to the slab, i.e. $\theta = 0$, which was chosen in the experiments and numerical simulations. This is expected since in this situation the boundary restricts diffusion along the gradient direction the most.

The signals are presented in Fig. 4. At low gradients, the Gaussian phase approximation is valid with an effective diffusion coefficient D . Note, however, the deviation from the free diffusion signal $E = e^{-bD_0}$ due to restriction by the slab. A short-time analysis [9,43–45] yields an apparent diffusion coefficient

$$D \approx D_0 \left(1 - \eta \frac{4}{3\sqrt{\pi}} \frac{S}{V} \sqrt{D_0 T} \right), \quad (23)$$

where S/V is the surface-to-volume ratio of the confining domain ($S/V = 2/L$ for a slab), $\eta \approx 0.9$ is a numerical prefactor that depends on the sequence [45], and $T = \Delta + \delta$ is the duration of the gradient sequence. This is a short-time approximation in the sense that $\eta\sqrt{D_0 T}/L$ should be small enough. In addition, this formula relies on the Gaussian phase approximation which requires small b -values. For our parameters, we get $D \approx 0.66D_0$ and the agreement between e^{-bD} and the signal at low gradients is good.

Additionally, we computed the kurtosis correction term from the cumulant expansion. Two different methods were used: (i) we evaluated the second derivative of the logarithm of the computed signal with respect to b by fitting the low- b part ($bD_0 < 1$) of $\log(E)$ by a quadratic polynomial; (ii) we searched for a value of the kurtosis that would fit best the computed signal over the largest range of b -values. The second method yielded a value of the kurtosis twice as large compared to the first method and a much better visual agreement with the theoretical and experimental curves. In Fig. 4, we show the result of the second method. One

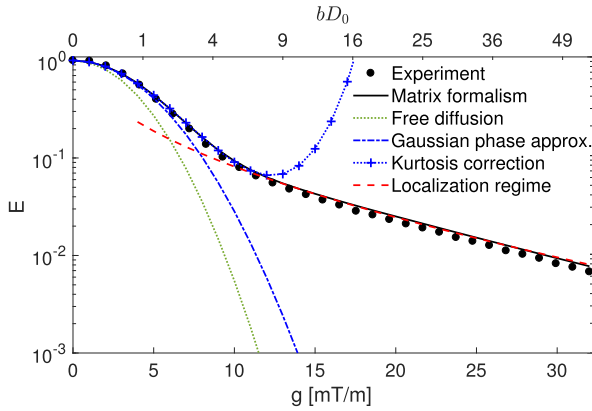


Fig. 4. Signal attenuation for phantom 1 (a slab of width 3 mm). Experimental results are shown by full circles and matrix formalism computation by a solid line. The signal for free diffusion e^{-bD_0} is indicated by a dotted line, whereas the low- b , short-time approximation e^{-bD} , where D is given by Eq. (23), is plotted as a dashed-dotted line. We also plot the cumulant expansion with kurtosis correction as dotted line with pluses. The high-gradient asymptotic formula (24) of the localization regime appears as a dashed line.

can see that the signal is well fitted up to $bD_0 \approx 6-7$, then the localization regime emerges and the cumulant expansion diverges very fast from the theoretical and experimental curves. The deviation of the cumulant expansion from the signal occurs at smaller b -values when we use the kurtosis computed from the first method (not shown). For clarity of the figures, we do not show the kurtosis correction for the other geometries. Note that in the narrow-pulse, short diffusion time limit, the kurtosis may be computed exactly as a function of the surface-to-volume ratio of the geometry [46].

At higher gradients, the signal follows the asymptotic decay (see Eq. (17) and Refs. [3,8–11])

$$E_{\text{slab}} \approx 2C_{1,1} \exp(-|a'_1| \ell_g^2 / \ell_s^2), \quad (24)$$

where the prefactor $C_{1,1}$ can be computed exactly [10,12] and scales as ℓ_g/L . One can interpret this prefactor as the fraction of spins inside the two layers of thickness $\sim \ell_g$ where the signal is localized. As we discussed in Section 2.4, $C_{1,1}$ decreases with increasing diffusion step duration $\Delta - \delta$. Note that the localization regime emerges at gradients as small as 10 mT/m, for which $\ell_s/\ell_g \approx 1.3$ and $bD_0 \approx 6$ (we recall that $bD_0 = (\Delta/\delta - 1/3)(\ell_s/\ell_g)^6$). Since the width of the slab is much greater than ℓ_g , one can treat the localization layers on both sides of the slab as independent from each other (see Fig. 1 and the discussion in Section 2.3).

We observe a remarkable agreement between the experimental data, exact solution via the matrix formalism, and the asymptotic relation (24). Note that the latter contains no fitting parameter (the prefactor $C_{1,1}$ was found by computing the eigenmodes numerically). Systematic minor deviations of the experimental points may be caused by weak misalignment of the gradient direction (i.e. θ slightly different from 0 in Eq. (22)) or weak surface relaxivity. Note that we performed all computations with a rectangular gradient profile instead of a trapezoidal one (in other words, with $\epsilon = 0$, see Fig. 3) and we checked that not accounting for the trapezoidal profile had a negligible influence on the computed signal due to the very short ramp-up time ($\epsilon = 0.34$ ms).

4.2. Diffusion inside a cylinder

If the diameter of the cylinder is much larger than the gradient length ℓ_g and the diffusion length ℓ_s , then the cylinder geometry is locally similar to the slab geometry except for the smaller “localization pocket” where the magnetization does not vanish. An argu-

ment similar to that of Eq. (22) implies that the magnetization is localized where the angle between the gradient and the normal vector to the boundary is close to 0 (this condition becomes more and more restrictive at higher b -values according to Eqs. (22) and (24)). The transverse magnetization inside a cylinder, obtained with a matrix formalism computation, supports this argument (Fig. 5). In fact, as the gradient increases, the magnetization gradually transforms from a flat uniform profile to the one that is localized around two opposite points on the boundary of the cylinder and displays two independent pockets at sufficiently high gradients.

In Fig. 6 we show the signal for diffusion inside a cylinder of diameter 3.8 mm. Although the signal decays faster than in the slab, one observes a similar stretched-exponential behavior. Using Eqs. (14) and (17), one gets the asymptotic decay for the cylinder:

$$E_{\text{cyl}} \approx C \exp\left(-|a'_1| \frac{\ell_g^2}{\ell_s^2} - \frac{\ell_s^2}{R^{1/2} \ell_g^{3/2}} + \frac{\sqrt{3} \ell_s^2}{2|a'_1| R \ell_g}\right), \quad (25)$$

where C is given by Eq. (18). Here, R is large enough so that there is no overlapping between the first two eigenmodes, and $C = 2C_{1,1}$. The prefactor $C_{1,1}$ can be computed numerically from the eigenmodes and scales approximately as $(\ell_g/R)^{7/4}$ (see Appendix A). One observes the perfect agreement between experiment, matrix formalism computation, and asymptotic formula at high gradients (without any fitting parameter). Note also that Eq. (24) with only the leading term is not accurate (not shown) so that the correction terms in the exponential are indeed important.

For a cylinder of a smaller diameter ($2R = 2$ mm, see Fig. 7), the signal shows some oscillations that are reminiscent of diffusion-diffraction patterns [14,38,47–49]. This is the case discussed in Section 2.3 where two localization pockets overlap because $\ell_g/(2R)$ is not small enough. The signal is still given by Eq. (25) but one cannot neglect the cross-term $C_{1,2}$ in the expression (18) of C . The oscillations are then described by $C_{1,2}$ and appear on top of the asymptotic stretched-exponential decay. These oscillations shown in Fig. 7 are very well reproduced by the asymptotic formulas (19) and (20) with $L = 2R$, where the coefficients μ_1 , μ_2 , and $\beta_{1,2}$ were computed numerically from the eigenmodes. These coefficients generally depend on g and $\beta_{1,2}$ additionally depends on the diffusion step duration $\Delta - \delta$. This overlapping phenomenon is supported by Fig. 8 which illustrates that the magnetization inside the cylinder is not well localized even at the highest gradient available.

4.3. Diffusion outside an array of rods

The geometry of phantoms 4 and 5 is defined by L , the center-to-center spacing between rods, and $2R$, the diameter of the rods. We consider three different cases: (a) phantom 4 ($L = 4$ mm and $2R = 3.2$ mm) with the gradient vector in the diagonal direction; (b) phantom 5 ($L = 3.4$ mm and $2R = 3.2$ mm) and gradient vector in the diagonal direction; (c) phantom 5 and gradient vector in the horizontal direction.

The main difference between these three cases is the spacing e_p between two neighboring rods along the gradient direction, i.e. the spacing between two neighboring localization pockets (see Fig. 9): $e_p = e_d = \sqrt{2}L - 2R = 2.5$ mm in (a); $e_p = e_d = 1.6$ mm in (b); and $e_p = e_h = 0.2$ mm in (c). Fig. 10 shows the signal for these three cases, ordered by descending e_p . Note that here the signal is formed by the magnetization localized near the rods and by the magnetization localized near the borders of the casing in which the phantom is enclosed. We did not plot the low- b , short time approximation $E = e^{-bD}$ here because the surface-to-volume ratio

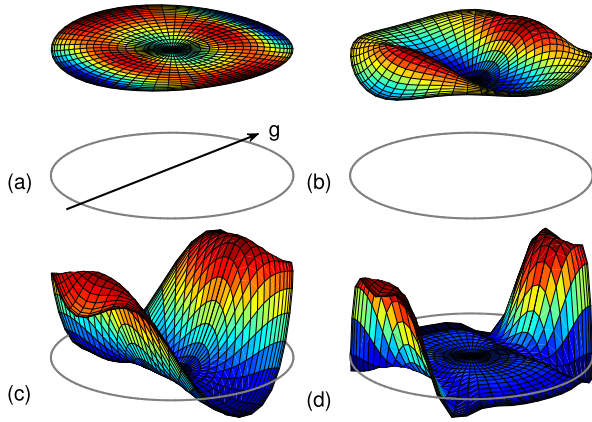


Fig. 5. Transverse magnetization computed by matrix formalism inside phantom 2 (a cylinder of diameter 3.8 mm) for four values of the gradient g : (a) 2 mT/m, (b) 5 mT/m, (c) 10 mT/m and (d) 32 mT/m. The direction of the gradient is indicated by an arrow.

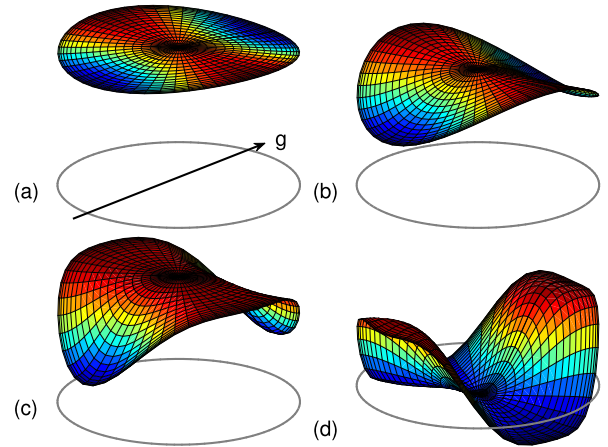


Fig. 8. Transverse magnetization computed by matrix formalism inside phantom 3 (a cylinder of diameter 2 mm) for four values of the gradient g : (a) 2 mT/m, (b) 5 mT/m, (c) 10 mT/m and (d) 32 mT/m. The direction of the gradient is indicated by an arrow.

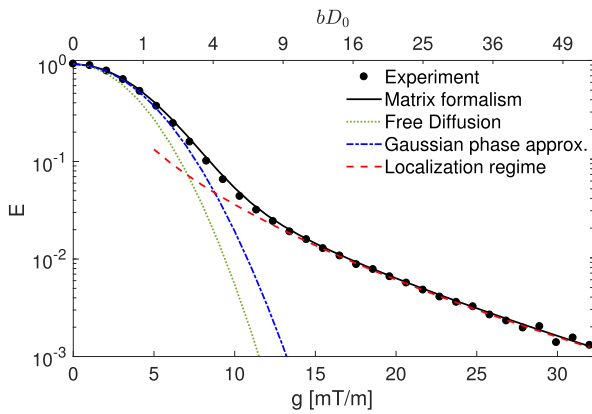


Fig. 6. Signal attenuation for diffusion inside phantom 2 (a cylinder of diameter 3.8 mm). Experimental results are shown by full circles and matrix formalism computation by a solid line. The signal for free diffusion is indicated by a dotted line, whereas the short-time approximation e^{-bD} , where D is given by Eq. (23), is plotted as a dashed-dotted line. The high-gradient asymptotic formula (25) of the localization regime appears as a dashed line.

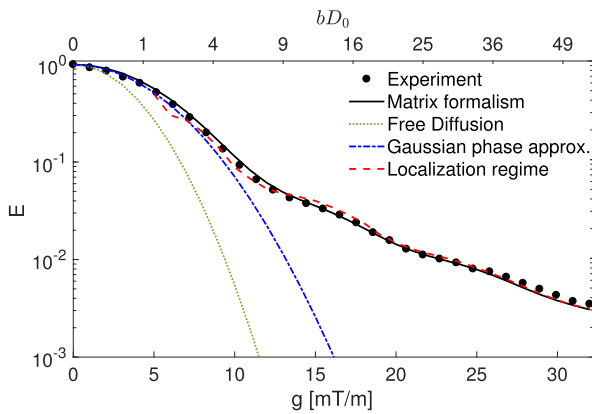


Fig. 7. Signal attenuation for diffusion inside phantom 3 (a cylinder of diameter 2 mm). Experimental results are shown by full circles and matrix formalism computation by a solid line. The signal for free diffusion is indicated by a dotted line, whereas the short-time approximation e^{-bD} , where D is given by Eq. (23), is plotted as a dashed-dotted line. The high-gradient asymptotic formula (25) of the localization regime appears as a dashed line.

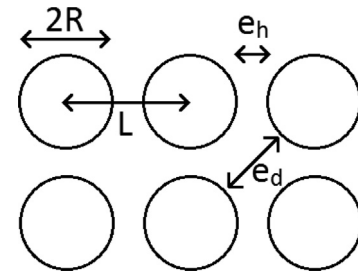


Fig. 9. Schematic representation of the rods showing the lengths e_d and e_h . The spacing e_p between two localized pockets is equal to e_d if the gradient is in the diagonal direction and to e_h if the gradient is in the horizontal or vertical direction.

of the structure is too large so that the approximate formula (23) for D is not valid.

First of all, one can note an excellent agreement between experimental data and Monte Carlo simulations. The high- g asymptotic behavior of the eigenvalues and the signal in a rods geometry is similar to the one for cylinders in Eq. (25) except for a sign change due to the opposite curvature [24]:

$$E_{\text{rods}} \approx C \exp \left(-|a'_1| \frac{\ell_\delta^2}{\rho_g^2} - \frac{\ell_\delta^2}{R^{1/2} \rho_g^{3/2}} - \frac{\sqrt{3} \ell_\delta^2}{2|a'_1| R \ell_g} \right), \quad (26)$$

where C is given by Eq. (18) and may be computed numerically from the eigenmodes. This formula matches very well the signal at high gradients in case (a) (see Fig. 10(a)).

In the previous subsection, we already saw the signal without oscillations (Fig. 6) due to well-localized states, as well as the signal with oscillations (Fig. 7) due to a partial overlap of two localization pockets when the size of the confining domain is not very large compared to ℓ_δ and ℓ_g . Here the same phenomenon occurs. With e_p much larger than ℓ_g (case (a)), there is little overlapping between the localization pockets of neighboring rods. This ensures the localization of the eigenmodes and the small amplitude of the oscillations in the signal (see Section 2.3), i.e. the validity of $C = 2C_{1,1}$. In the case where the ratio between e_p and ℓ_g is smaller, i.e. localization pockets overlap more (case (b)), more pronounced oscillations on top of the overall decay (26) arise (see Fig. 10(b)). The signal is still described by Eq. (26), and the oscillations are contained in the cross-term $C_{1,2}$ from the expression (18) of C and may be computed from Eqs. (19) and (20) (with $L = e_p$). Systematic

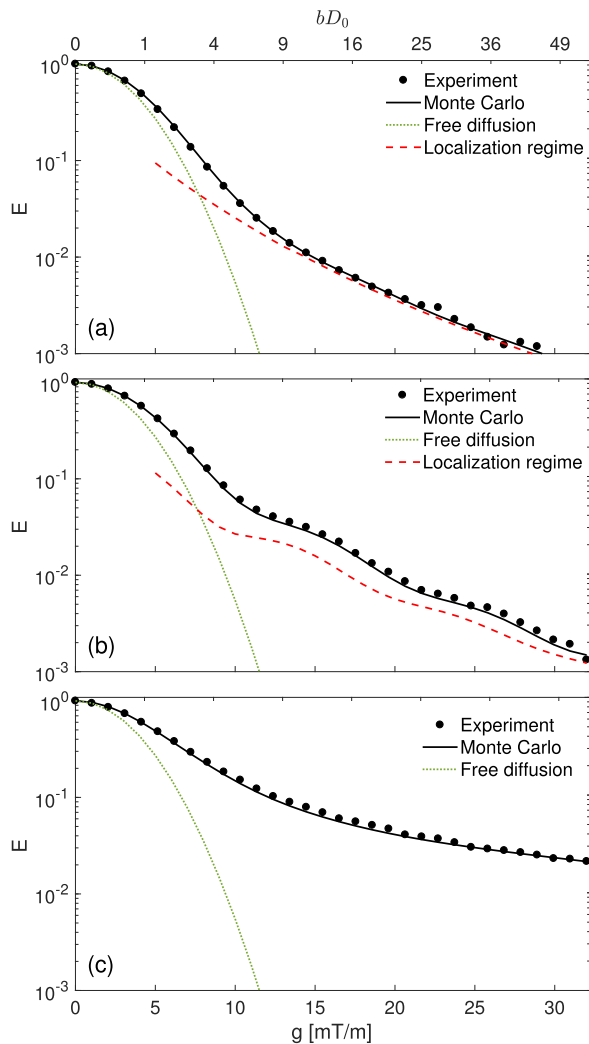


Fig. 10. Signal attenuation for diffusion in phantoms 4 and 5 (array of rods of diameter 3.2 mm and center-to-center spacing 4 mm and 3.4 mm, respectively). (a) phantom 4 with the gradient in the diagonal direction, spacing $e_p = 2.5$ mm; (b) phantom 5 and diagonal gradient direction, spacing $e_p = 1.6$ mm; (c) phantom 5 and horizontal gradient direction, spacing $e_p = 0.2$ mm. Experimental results are shown by full circles and Monte Carlo simulations by a solid line. The signal for free diffusion is indicated by a dotted line. The high-gradient asymptotic formula (26) of the localization regime appears as a dashed line. The latter is not shown for (c) as this regime is not applicable here, see the text.

deviations between the exact signal and the asymptotic formulas may be attributed to the truncation of Eq. (14), neglecting higher-order modes in the expression of the signal, and not accounting for the borders in the experimental setup.

In turn, in case (c) e_p is smaller than ℓ_g even at the highest gradient available. If one could approximate the small space between two neighboring rods as a slab, then the ratio ℓ_g/e_p would be too large for localization to be relevant (see Section 2.3). Our conjecture is that the residual signal at high gradients may be interpreted as a kind of motional narrowing regime (see [3,50]) inside the small gaps of width e_p between the rods.

5. Discussion and conclusion

We have observed and described the localization regime in three geometries: slab, cylinder, and array of circular obstacles

(rods). The localization regime appears whenever the gradient length $\ell_g = (D_0/G)^{1/3}$ is much smaller than the diffusion length $\ell_\delta = (D_0\delta)^{1/2}$ and any relevant geometrical length scale ℓ_s of the medium along the gradient direction. Thus, it is universal at high gradients and non-narrow pulses. In this regime, the transverse magnetization is localized near the obstacles, boundaries, or membranes of the sample. For this reason, the signal is particularly sensitive to the microstructure of the medium. In particular, possible oscillations of the signal are caused by a partial overlap between localized magnetization pockets and thus contain information about mutual arrangements of obstacles.

Let us clarify the role of the conditions (i) $\ell_g \ll \ell_\delta$ and (ii) $\ell_g \ll \ell_s$. Condition (i) ensures that the eigenmode decomposition of the transverse magnetization may be truncated to its first terms. In turn, the signal decays exponentially with δ and its dependence on g is essentially determined by the first eigenvalue of the Bloch-Torrey operator. Furthermore, condition (ii) is necessary for the localization of the eigenmodes of the Bloch-Torrey operator and the validity of the high- g expansion of its eigenvalues. Thus, both conditions are required for the localization of the transverse magnetization and the stretched-exponential decay of the signal with g .

An extreme case where condition (i) is not satisfied would be the narrow pulses limit ($g \rightarrow \infty$ and $\delta \rightarrow 0$). Although these experiments require high gradients, they do not achieve the localization regime. In fact, whereas the localization regime emerges when $G^2\delta^3D_0 \gg 1$, narrow-pulse experiments correspond to $G \rightarrow \infty$ and $\delta \rightarrow 0$ such that $G\delta = q$ is a finite value. This leads to $G^2\delta^3D_0 \rightarrow 0$. In other words, the signal attenuation is not produced by the encoding step but by the subsequent diffusion step with $g = 0$. This is evident from the fact that the signal is left unchanged if one sets $\Delta = 0$, i.e. no diffusion time between two short gradient pulses. On the other hand, condition (ii) is typically not satisfied in the motional narrowing regime ($g \rightarrow 0$ and $\delta \rightarrow \infty$). Here, the eigenmodes of the Bloch-Torrey operator are close to the eigenmodes of the Laplace operator. In particular, the first Laplacian eigenmode is constant if one assumes impermeable, non-relaxing boundaries. Therefore, the transverse magnetization at long times is uniform inside the sample.

Slab and cylinder are confined geometries that may model an intracellular space. It is well-known that such domains produce non-Gaussian signals, for example in the limit of narrow pulses (e.g. diffusion-diffraction patterns, see [14,38,47–49]). However, in most former studies the signal from the extracellular space was assumed to be Gaussian, and non-Gaussian effects were attributed to multiple contributing pools. In other words, one assumes either that the b -values are sufficiently small so that the Gaussian phase approximation is applicable or that the obstacles may be treated as an effective medium with an effective diffusivity D such that the diffusion process is Gaussian. The latter assumption is in principle valid only in the very long time limit, as it has been discussed for weak diffusion weighting, e.g. in Refs. [51,52]. Our measurements reveal the non-Gaussianity of the extracellular signal at high gradients and we have shown that it simply results from the localization of the magnetization at the outer boundaries of the obstacles. Ignoring this effect may lead to false interpretations created by commonly used fitting models.

We stress that the localization regime in our setting starts to emerge with moderate gradients of about 10 mT/m, or at bD_0 about 6. These conditions are easily achieved in most clinical scanners. Note that the localization regime emerges under the condition $\ell_\delta/\ell_g \gg 1$ which can be restated as $bD_0 \propto \gamma^2D_0g^2\delta^3 \gg 1$. In order to rescale the experimental conditions from xenon gas to water, we compute the ratio $(\gamma^2D_0)_{\text{xenon}}/(\gamma^2D_0)_{\text{water}} \approx 10^3$. This

means that in order to have the same value of $\gamma^2 D_0 g^2 \delta^3$, one has to increase g and δ such that $g^2 \delta^3$ is 10^3 times larger with water than with xenon. For example, the experiments by Hürlimann et al. were performed with $\delta = 60$ ms which is approximately 10 times longer than in our experiments, and gradients of comparable magnitude as ours (around 20 mT/m).

Theoretical aspects of diffusion NMR have been broadly explored at weak gradients by means of perturbation theory. While surface-to-volume ratio, overall curvature, permeability and surface relaxivity could be estimated at short times [43–45], the structural organization of barriers is accessible at long times [51,52]. In biomedical applications, the apparent diffusion coefficient and kurtosis are employed as biomarkers to detect stroke, tumors, lesions, partial tissue destruction, etc. (see [19] and references therein). In spite of its considerable progress in medicine and material sciences, the comprehensive theory of diffusion NMR remains to be elaborated. The recent mathematical advances show that the gradient term presents a singular perturbation to the Laplace operator in unbounded domains, resulting in the discrete spectrum of the Bloch-Torrey operator [25]. But even in bounded domains, the presence of the gradient term may lead to branching points of the spectrum and thus a finite radius of convergence of the cumulant expansion [8]. As we have shown, these mathematical facts bring interesting new physics in the regime of strong and wide gradient pulses, where the conventional perturbation theory fails and non-perturbative approaches are necessary. Even so the localization regime is only partly understood and exploiting its potential advantages is still challenging in experiments (partly due to strongly attenuated signals), the high sensitivity of the signal to the microstructure at strong gradients is a promising avenue for creating new experimental protocols. If former theoretical efforts were essentially focused on eliminating the dephasing effects and reducing the mathematical problem to the computation of the diffusion propagator and related quantities, future developments have to aim at exploiting the advantages of high gradients.

Acknowledgments

N.M. and D.S.G. acknowledge Bernard Helffer for fruitful discussions.

Appendix A. Asymptotic behavior of the magnetization for curved boundaries

In this section we provide additional insights onto the behavior of the magnetization at an almost flat boundary with curvature radius R_c going to infinity. For simplicity we assume a 2D geometry but the computation can be extended to the 3D case (see below). We compare two limits that both correspond to $R_c \rightarrow \infty$: (i) the diffusion length ℓ_δ is very small so that one can use a local effective gradient approach where the curved boundary is treated as a collection of multiple flat boundaries with different angles and positions; (ii) the gradient length ℓ_g is very small so that the eigenmodes of the Bloch-Torrey operator are localized at the boundary. In both cases we consider an initial uniform magnetization $M_0(\mathbf{r}) = 1$ and we apply a *single* rectangular gradient pulse of amplitude g and duration δ .

As we consider the limit of large curvature radius compared to other scales, we can locally treat the boundary as a circular arc of radius $|R_c|$. We introduce the polar coordinates (r, θ) , where $r = 0$ at the center of the circular arc and $\theta = 0$ at the point where the gradient is orthogonal to the boundary (i.e. where localization occurs). Without loss of generality, we assume that the gradient

is directed along $\theta = 0$. The situation where the gradient is along $\theta = \pi$ is essentially identical with some sign changes. We have then

$$x = r \cos \theta - |R_c| \quad y = r \sin \theta, \quad (\text{A.1})$$

so that $(x, y) = (0, 0)$ is at the localization point.

A.1. Local effective gradient approach

After the gradient pulse, the local magnetization at the boundary is shaped by two different effects: attenuation due to diffusion along the gradient, and dephasing due to x being non zero along the boundary. The diffusion effect is obtained from an argument similar to Eq. (22): the component $g \cos \theta$ perpendicular to the boundary produces a localization-type attenuation whereas the component $g \sin \theta$ parallel to the boundary produces a free diffusion-type attenuation. This results in the formula

$$M(\mathbf{r}, \delta) \approx e^{-iG\delta|R_c|(1-\cos\theta)} e^{-\frac{1}{3}D_0G^2\delta^3\sin^2\theta} M_{\text{loc}}(r, g \cos \theta, \delta),$$

where M_{loc} denotes the magnetization attenuated by the component of the gradient perpendicular to the boundary. Typically, at high gradients, one has $M_{\text{loc}}(r, g, \delta) \propto \nu_1(r) \exp(-|a_1| \ell_\delta^2 / \ell_g^2)$, where $\nu_1(r)$ can be expressed in terms of Airy functions. In the localization regime, $D_0G^2\delta^3$ takes large values so that one can neglect the magnetization at large angles and get the approximate formula

$$M(\mathbf{r}, \delta) \approx e^{-iG\delta R_c \theta^2 / 2} e^{-D_0G^2\delta^3 \theta^2 / 3} M_{\text{loc}}(r, g, \delta).$$

Since the magnetization is non zero only at small angles, one can identify the polar coordinates r and θ with the Cartesian coordinates x and $y/|R_c|$, respectively. The magnetization is then the product of a function of x and a function of y :

$$M(\mathbf{r}, \delta) \approx M_{\text{loc}}(x, g, \delta) \exp\left(-i \frac{\ell_\delta^2 y^2}{2\ell_g^3 |R_c|} - \frac{\ell_\delta^6 y^2}{3\ell_g^6 |R_c|^2}\right). \quad (\text{A.2})$$

The above formula reveals that at large R_c the diffusion effect is much weaker than the dephasing effect. Both effects vanish in the limit $R_c \rightarrow \infty$ and one recovers the magnetization for a flat boundary.

A.2. Eigenmode summation

The above reasoning is intuitive and gives the correct limit. However, the result seems paradoxical with Eq. (14) that implies that a large R_c produces a nearly continuous spectrum, as opposed to the simple formula (12) which is exact for the flat boundary. In this section, we present an approximate computation of the eigenmodes in the limit $\ell_g \ll R_c$ and we show how these eigenmodes can be summed in order to recover the result of the previous subsection in the short-time regime.

The Bloch-Torrey equation in polar coordinates is:

$$\frac{\partial M}{\partial t} = D_0 \left(\frac{\partial^2 M}{\partial r^2} + \frac{1}{r} \frac{\partial M}{\partial r} + \frac{1}{r^2} \frac{\partial^2 M}{\partial \theta^2} \right) - iG(r \cos \theta - |R_c|)M. \quad (\text{A.3})$$

We study the regime where the magnetization is localized over a small width $\ell_g \ll |R_c|$ in the radial direction, and over small angles $\theta \ll 1$, thus we approximate the above equation as

$$\begin{aligned} \frac{\partial M}{\partial t} &= D_0 \left(\frac{\partial^2 M}{\partial r^2} + \frac{1}{r} \frac{\partial M}{\partial r} \right) - iG(r - |R_c|)M \\ &+ D_0 \frac{1}{R_c^2} \frac{\partial^2 M}{\partial \theta^2} + iG|R_c| \frac{\partial^2 M}{\partial \theta^2}. \end{aligned} \quad (\text{A.4})$$

The variables r, θ are now separated and we can study each one independently by writing $M(r, \theta, t) = f(r, t)h(\theta, t)$. The radial part

differs from the one-dimensional Bloch-Torrey equation by the term $(D_0/r)\partial M/\partial r$, which introduces a correction term of the order of $D_0/(l_g R_c)$ in the eigenvalues (this is the third term of the asymptotic expansion (14)¹).

The angular part is the Bloch-Torrey equation with a parabolic magnetic field [53], or equivalently a quantum harmonic oscillator with imaginary potential [26]. Let us introduce the variable $y = |R_c|\theta$. We can rewrite the angular part of the above equation as

$$\frac{\partial h}{\partial t} = D_0 \frac{\partial^2 h}{\partial y^2} + i \frac{G}{2|R_c|} y^2 h.$$

By multiplying y by $e^{-i\pi/8}$, one obtains the quantum harmonic oscillator with a real potential. Hence, the eigenvalues λ_l and eigenmodes h_l are given by

$$h_l(y) = K_l \exp\left(-e^{-i\pi/4} \frac{y^2}{2\ell_{g,\parallel}^2}\right) H_{l-1}\left(e^{-i\pi/8} \frac{y}{\ell_{g,\parallel}}\right), \quad (\text{A.6})$$

$$\lambda_l = (2l-1)e^{-i\pi/4} \ell_{g,\parallel}^{-2}, \quad (\text{A.7})$$

$$K_l = \frac{e^{-i\pi/16}}{\pi^{1/4} \ell_{g,\parallel}^{1/2} (2^{l-1} (l-1)!)^{1/2}}, \quad (\text{A.8})$$

$$\ell_{g,\parallel} = (2D_0|R_c|/G)^{1/4} = (2\ell_g^3|R_c|)^{1/4}, \quad (\text{A.9})$$

where $l = 1, 2, \dots$ and H_{l-1} are Hermite polynomials (in particular, $H_0(z) = 1$). One recognizes in the formula for λ_l the second term of the asymptotic expansion (14).

In three dimensions, the boundary is locally described by two principal radii of curvature $R_{c,1}$ and $R_{c,2}$ associated with two orthogonal coordinate axes (y_1, y_2) . The radial coordinate r is now defined as the algebraic distance from the surface with a given sign convention (positive on one side and negative on the other).² The Bloch-Torrey equation splits into three equations: one for the radial part of the magnetization and two equations similar to Eq. (A.5) (where (y, R_c) is replaced by $(y_1, R_{c,1})$ or $(y_2, R_{c,2})$) for the lateral part of the magnetization. The lateral eigenmodes are thus given by products $h_{l_1}(y_1)h_{l_2}(y_2)$ with eigenvalues $\lambda_{l_1} + \lambda_{l_2}$, for all pairs of positive integers (l_1, l_2) , which yields the second term of the asymptotic formula (15). In order to obtain the third term of Eq. (15), one needs to compute the radial part of the Laplacian in the coordinate system (r, y_1, y_2) , which yields for $r \ll |R_{c,1}|, |R_{c,2}|$:

$$\nabla^2 M = \nabla \cdot \left(\frac{\partial M}{\partial r} \mathbf{e}_r \right) = \frac{\partial^2 M}{\partial r^2} + \left(\frac{1}{R_{c,1}} + \frac{1}{R_{c,2}} \right) \frac{\partial M}{\partial r}. \quad (\text{A.10})$$

Similarly to the 2D case, the second term of the Laplacian yields the third term of Eq. (15).

As one can see from the expression of the eigenmodes h_l , $\ell_{g,\parallel}$ is the length scale of localization *parallel to the boundary* (and perpendicular to the gradient). Note that $\ell_{g,\parallel} > \ell_g$ since we assumed $\ell_g \ll |R_c|$. To this length one can associate a time $t_{g,\parallel} = \ell_{g,\parallel}^2/(2D_0)$. Localization parallel to the boundary occurs when $\ell_\delta \gg \ell_{g,\parallel}$, i.e., $\delta \gg t_{g,\parallel}$. In three dimensions, one would have two lengths $\ell_{g,\parallel}$ corresponding to the two local principal radii of curvature of the boundary.

The magnetization after the gradient pulse may be computed either from the summation of the eigenmodes or directly from Eq. (A.5):

$$M(y, \delta) = \sum_{l=1}^{\infty} \left(\int_{-\infty}^{\infty} h_l(y') dy' \right) h_l(y) e^{-\lambda_l D_0 \delta} \quad (\text{A.11})$$

$$= \frac{\exp(-e^{i\pi/4} \tanh(e^{i\pi/4} \delta/t_{g,\parallel}) y^2 / (2\ell_{g,\parallel}^2))}{\cosh(e^{i\pi/4} \delta/t_{g,\parallel})^{1/2}}. \quad (\text{A.12})$$

The magnetization after the gradient pulse is a complex Gaussian function of y . Its width decreases from ∞ to $\ell_{g,\parallel}$ when δ increases from 0 to ∞ . Thus in the long-time limit we get a localized magnetization pocket parallel to the boundary, and $\ell_{g,\parallel}$ is the width of the pocket. Note that the magnetization in the long-time limit is exactly given by the first eigenmode $h_1(y)$ computed above, multiplied by the exponential decay $\exp(-\lambda_1 D_0 \delta)$. Since the pocket is localized over a length $\sim \ell_g$ along the gradient direction and over $\sim \ell_{g,\parallel}$ perpendicular to the gradient, its area is proportional to $\ell_g \ell_{g,\parallel}$, which scales as $\ell_g^{7/4} |R_c|^{1/4}$. Thus the prefactor $C_{1,1}$ scales approximately as $\ell_g^{7/4}$ for a curved boundary. In three dimensions one would get the scaling $\ell_g^{10/4}$.

What remains to show is that we recover Eq. (A.2) in the appropriate limit. For the local effective gradient approach to be valid, one needs *a priori* sufficiently short diffusion times. Indeed, the formula (A.12) becomes in the short-time limit:

$$M(y, \delta) \underset{\delta/t_{g,\parallel} \ll 1}{=} \exp\left(-i \frac{y^2 \delta}{2\ell_{g,\parallel}^2 t_{g,\parallel}} - \frac{y^2 \delta^3}{3\ell_{g,\parallel}^2 T^3}\right), \quad (\text{A.13})$$

which yields the same lateral magnetization as in the formula (A.2).

Thus we have several regimes for the magnetization at high gradients, as shown on Fig. A.11 where we increase δ at fixed G . If $\ell_g \ll |R_c|$, then there is a separation of scales between ℓ_g and $\ell_{g,\parallel}$ and in turn between t_g and $t_{g,\parallel}$. Thus localization along the gradient occurs at a much smaller time δ than localization perpendicular to

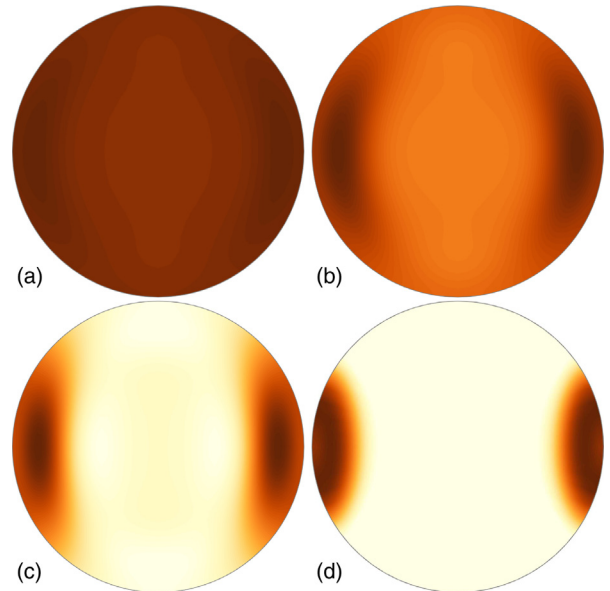


Fig. A.11. Real part of the transverse magnetization for increasing pulse duration δ computed by matrix formalism inside a disk of radius $R_c = 1.9$ mm (phantom 2) and the gradient $g = 32$ mT/m in the left-right direction (this gradient corresponds to $R_c/\ell_g \approx 8$ and thus $\ell_{g,\parallel} \approx 2\ell_g$). For simplicity, we assume that there is no gap between two gradient pulses: $\Delta = \delta$. The magnetization is shown by color code, with white for zero magnetization and dark brown for high magnetization. (a) $\ell_\delta/\ell_g = 0.84$: the magnetization is nearly uniform inside the disk; (b) $\ell_\delta/\ell_g = 1.1$: the magnetization starts to localize along the gradient direction but remains nearly uniform along the boundary; (c) $\ell_\delta/\ell_g = 1.3$: the magnetization is completely localized along the gradient direction and starts to shrink along the boundary; (d) $\ell_\delta/\ell_g = 2.0$ (so that $\ell_\delta/\ell_{g,\parallel} = 1.0$): the magnetization is localized both along the gradient (with size ℓ_g) and perpendicular to the gradient (with size $\ell_{g,\parallel}$).

¹ Note that $R_c > 0$ (concave boundary) corresponds to the domain $r < |R_c|$ and $R_c < 0$ (convex boundary) corresponds to the domain $r > |R_c|$. Thus, in our formulas the sign of R_c enters implicitly through the orientation of the unit vector \mathbf{e}_r with respect to the boundary, which in turn affects the sign of $\partial M/\partial r$.

² The sign of $R_{c,1}$, $R_{c,2}$ is conventional; here we evaluate it by looking at the surface from the $r < 0$ domain.

the gradient. In particular, if $t_g < \delta < t_{g,\parallel}$, the magnetization is localized along the gradient direction and delocalized along the boundary, as described by Eq. (A.2). Note that panel (d) of Fig. A.11 corresponds to our experimental value of δ . The larger $|R_c|$, the longer $t_{g,\parallel}$ thus in the limit $|R_c| \rightarrow \infty$, one only gets localization along the gradient direction. In this limit, the spectrum of the Bloch-Torrey operator is getting denser and denser due to decreasing spacing between eigenvalues λ_l , $l = 1, 2, \dots$. We have shown that by summing these lateral modes, one obtains the expected Gaussian contribution in the lateral direction, where the dephasing effect dominates over the diffusion attenuation.

Appendix B. Some clarifications on the spectrum of a differential operator

Physicists and mathematicians employ the word “spectrum” with different meanings, which may lead to some confusion. In this section, we illustrate by examples the mathematical definition of the spectrum and its distinction from a physical one. We shall see that in the end it is mostly consistent with the physicists’ point of view and that according to this definition, the spectrum of the Bloch-Torrey operator is *empty* in free space. We do not claim for mathematical rigor here.

Let us consider a differential operator \mathcal{A} . This operator is defined for functions with some prescribed properties (smoothness, boundary conditions, etc.). Moreover, for technical reasons, one often restricts the operator to square-integrable functions $u \in L_2$. All these conditions define the domain $\mathcal{D}_{\mathcal{A}}$ of the operator.

An eigenmode (also called eigenmode, or eigenvector, or eigenstate) of \mathcal{A} is a function $u_\lambda \in \mathcal{D}_{\mathcal{A}}$ such that $\mathcal{A}u_\lambda = \lambda u_\lambda$, where $\lambda \in \mathbb{C}$ is the corresponding eigenvalue. Mathematically, the spectrum of \mathcal{A} , denoted $\sigma(\mathcal{A})$ is not the set of eigenvalues of \mathcal{A} but a larger set: it is the set of all $\lambda \in \mathbb{C}$ such that $\mathcal{A} - \lambda$ is not invertible [26]. The eigenvalues present a particular case in which $\mathcal{A} - \lambda$ is not injective and thus form a subset of the spectrum; both definitions are not equivalent in (infinite dimensional) functional spaces. In particular, as we shall discuss below, the set of eigenvalues may be empty even though the spectrum is not.

As an example, let us consider the Laplace operator on \mathbb{R} , $\mathcal{A} = -d^2/dx^2$, whose spectrum is $[0, \infty)$ from the physicists’ point of view. We shall see that it is also the case according to the mathematical definition of $\sigma(\mathcal{A})$. Solving the equation $\mathcal{A}u = \lambda u$ with $\lambda \in \mathbb{R}$ yields

$$u_\lambda(x) = \exp(\pm i\lambda^{1/2}x) \quad \text{if } \lambda \geq 0, \quad (\text{B.1})$$

$$u_\lambda(x) = \exp(\pm |\lambda|^{1/2}x) \quad \text{if } \lambda \leq 0. \quad (\text{B.2})$$

None of these solutions are square-integrable, hence they do not belong to $\mathcal{D}_{\mathcal{A}}$ and they are not eigenmodes of \mathcal{A} in the mathematical sense. If $\lambda < 0$, then $u_\lambda(x)$ diverges exponentially at ∞ or $-\infty$. If $\lambda \geq 0$, $u_\lambda(x)$ does not diverge at $\pm\infty$ and is in fact a tempered distribution. One can then see $u_\lambda(x)$ as a linear form on $\mathcal{D}_{\mathcal{A}}$ that satisfies an eigenmode equation. Therefore, u_λ with $\lambda \geq 0$ is a “generalized eigenmode”, and

$$\forall v \in \mathcal{D}_{\mathcal{A}}, \langle u_\lambda, (\mathcal{A} - \lambda)v \rangle = \langle (\mathcal{A} - \lambda)u_\lambda, v \rangle = 0, \quad (\text{B.3})$$

so that the range of $\mathcal{A} - \lambda$ is included in the orthogonal space of u_λ , thus $\mathcal{A} - \lambda$ is not surjective and $\lambda \in \sigma(\mathcal{A})$. Another way to prove this result is to construct an approximate eigenmode by multiplying $u_\lambda(x)$ by a sequence of finitely supported functions with increasing support. The fact that $u_\lambda(x)$ does not diverge at $\pm\infty$ allows one to control the above approximation and prove that $\lambda \in \sigma(\mathcal{A})$. Note that we did not consider the case where λ is not real since \mathcal{A} is Hermitian (or self-adjoint). It is easy to see from the general form of $u_\lambda(x)$

$$u_\lambda(x) = \exp(\pm i\lambda^{1/2}x), \quad \lambda \in \mathbb{C} \quad (\text{B.4})$$

that $u_\lambda(x)$ diverges at ∞ or $-\infty$ whenever $\text{Im}(\lambda) \neq 0$. One concludes here that the operator $\mathcal{A} = -d^2/dx^2$ has a continuous spectrum.

Now we discuss the case of the one-dimensional Bloch-Torrey operator on \mathbb{R} : $\mathcal{A} = d^2/dx^2 - ix$. As we shall see, this operator exhibits an empty spectrum (note that the spectrum of an Hermitian operator is never empty). We apply the same procedure as in the previous example and look for solutions of the equation $\mathcal{A}u_\lambda = \lambda u_\lambda$:

$$u_\lambda(x) = \text{Ai}(e^{i\pi/6}(x - i\lambda)) \quad \text{or} \quad u_\lambda(x) = \text{Bi}(e^{i\pi/6}(x - i\lambda)), \quad (\text{B.5})$$

where $\text{Ai}(z)$ and $\text{Bi}(z)$ are Airy functions of the first and second kind. Both these functions (and any linear combination of them), for any $\lambda \in \mathbb{C}$, exhibit a fast divergence (as an exponential of $|x|^{3/2}$) at $-\infty$ or ∞ hence they cannot be generalized eigenmodes. From another point of view, the divergence of $u_\lambda(x)$ at $-\infty$ or ∞ prohibits the construction of a sequence of approximate eigenmodes. The spectrum of \mathcal{A} is then empty.

One may argue that this is merely a matter of convention and that the spectrum of the Bloch-Torrey operator may be seen to be continuous (and in fact, equal to \mathbb{C}) if the rapidly diverging functions $u_\lambda(x)$ from Eq. (B.5) are allowed. However, to be consistent with this convention, one would also have to consider $u_\lambda(x)$ from Eq. (B.4), for any $\lambda \in \mathbb{C}$, as an eigenmode of the Laplace operator and the spectrum of the Laplace operator on \mathbb{R} would be \mathbb{C} . Therefore, to be consistent with the general convention that the spectrum of the Laplace operator on \mathbb{R} is $[0, \infty)$, one must conclude that the spectrum of the Bloch-Torrey operator on \mathbb{R} is empty. Note that this discussion extends to other domains in higher dimension.

References

- [1] P.T. Callaghan, *Principles of Nuclear Magnetic Resonance Microscopy*, first ed., Clarendon Press, 1991.
- [2] W. Price, *NMR Studies of Translational Motion: Principles and Applications*, Cambridge Molecular Science, 2009.
- [3] D.S. Grebenkov, NMR survey of reflected Brownian motion, *Rev. Mod. Phys.* 79 (2007) 1077–1137.
- [4] J. Pfeuffer, S.W. Provencher, R. Gruetter, Water diffusion in rat brain in vivo as detected at very large b values is multicompartmental, *MAGMA* 8 (1999) 98–108.
- [5] V.J. Wedeen, D.L. Rosene, R. Wang, G. Dai, F. Mortazavi, P. Hagmann, J.H. Kaas, W.-Y.I. Tseng, The geometric structure of the brain fiber pathways, *Science* 335 (6076) (2012) 1628–1634.
- [6] V.G. Kiselev, Fundamentals of diffusion MRI physics, *NMR Biomed.* 30 (3) (2017) e3602.
- [7] A.F. Fröhlich, L. Ostergaard, V.G. Kiselev, Effect of impermeable boundaries on diffusion-attenuated MR signal, *J. Magn. Reson.* 179 (2006) 223–233.
- [8] S.D. Stoller, W. Happer, F.J. Dyson, Transverse spin relaxation in inhomogeneous magnetic fields, *Phys. Rev. A* 44 (1991) 7459–7477.
- [9] T.M. de Swiet, P.N. Sen, Decay of nuclear magnetization by bounded diffusion in a constant field gradient, *J. Chem. Phys.* 100 (8) (1994) 5597–5604.
- [10] M.D. Hürlimann, K.G. Helmer, T.M. de Swiet, P.N. Sen, Spin echoes in a constant gradient and in the presence of simple restriction, *J. Magn. Res. A* 113 (2) (1995) 260–264.
- [11] D.S. Grebenkov, Diffusion MRI/NMR at high gradients: challenges and perspectives, *Micropor. Mesopor. Mater.* 269 (2018) 79–82.
- [12] D.S. Grebenkov, Exploring diffusion across permeable barriers at high gradients. II. Localization regime, *J. Magn. Reson.* 248 (Supplement C) (2014) 164–176.
- [13] D.S. Grebenkov, B. Helffer, R. Henry, The complex Airy operator on the line with a semipermeable barrier, *SIAM J. Math. Anal.* 49 (2017) 1844–1894.
- [14] P.T. Callaghan, A. Coy, D. MacGowan, K.J. Packer, F.O. Zelaya, Diffraction-like effects in NMR diffusion studies of fluids in porous solids, *Nature* 351 (1991) 467–469.
- [15] T. Niendorf, R.M. Dijkhuizen, D.G. Norris, M. van Lookeren Campagne, K. Nicolay, Biexponential diffusion attenuation in various states of brain tissue – implications for diffusion-weighting imaging, *Magn. Reson. Med.* 36 (1996) 847–857.
- [16] J.H. Jensen, J.A. Helpert, A. Ramani, H. Lu, K. Kaczynski, Diffusion kurtosis imaging: the quantification of non-Gaussian water diffusion by means of magnetic resonance imaging, *Magn. Reson. Med.* 53 (2005) 1432–1440.
- [17] R.E. Jacob, G. Laicher, K.R. Minard, 3D MRI of non-Gaussian $^3\text{H}_2$ gas diffusion in the rat lung, *J. Magn. Reson.* 188 (2007) 357–366.
- [18] F.B. Laun, T.A. Kuder, W. Semmler, B. Stieltjes, Determination of the defining boundary in nuclear magnetic resonance diffusion experiments, *Phys. Rev. Lett.* 107 (2011) 048102.

- [19] D.S. Novikov, S.N. Jespersen, V.G. Kiselev, E. Fieremans, Quantifying brain microstructure with diffusion MRI: theory and parameter estimation, *NMR Biomed.* 32 (2018) e3998.
- [20] D.A. Yablonskiy, J.L. Bretthorst, J.J.H. Ackerman, Statistical model for diffusion attenuated MR signal, *Magn. Reson. Med.* 50 (2003) 664–669.
- [21] D.S. Novikov, V.G. Kiselev, Effective medium theory of a diffusion-weighted signal, *NMR Biomed.* 23 (2010) 682–697.
- [22] F. Grinberg, E. Farrher, L. Ciobanu, F. Geffroy, D. Le Bihan, N.J. Shah, Non-Gaussian diffusion imaging for enhanced contrast of brain tissue affected by ischemic stroke, *PLOS One* 9 (2014) c89225.
- [23] H.C. Torrey, Bloch equations with diffusion terms, *Phys. Rev.* 104 (1956) 563–565.
- [24] D.S. Grebenkov, B. Helffer, On spectral properties of the Bloch-Torrey operator in two dimensions, *SIAM J. Math. Anal.* 50 (2018) 622–676.
- [25] Y. Almog, D.S. Grebenkov, B. Helffer, Spectral semi-classical analysis of a complex Schrödinger operator in exterior domains, *J. Math. Phys.* 59 (2018) 041501.
- [26] B. Helffer, *Spectral Theory and Its Applications*, Cambridge University Press, 2013.
- [27] N. Moiseyev, *Non-Hermitian Quantum Mechanics*, Cambridge University Press, 2011.
- [28] M. Herberthson, E. Özarslan, H. Knutsson, C.-F. Westin, Dynamics of local magnetization in the eigenbasis of the Bloch-Torrey operator, *J. Chem. Phys.* 146 (2017) 124201.
- [29] C.H. Ziener, T. Kampf, G. Reents, H.-P. Schlemmer, W.R. Bauer, Spin dephasing in a magnetic field, *Phys. Rev. E* 85 (2012) 051908.
- [30] C.H. Ziener, T. Kampf, H.-P. Schlemmer, L.R. Buschle, Spin echoes: full numerical solution and breakdown of approximative solutions, *J. Phys.: Condens. Matter* 31 (2019) 155101.
- [31] T.G. Walker, W. Happer, Spin-exchange optical pumping of noble-gas nuclei, *Rev. Mod. Phys.* 69 (1997) 629–642.
- [32] A.-M. Oros, N.J. Shah, Hyperpolarized xenon in NMR and MRI, *Phys. Med. Biol.* 49 (20) (2004) R105–R153.
- [33] N.J. Shah, T. Ünlü, H.-P. Wegener, H. Halling, K. Zilles, S. Appelt, Measurement of rubidium and xenon absolute polarization at high temperatures as a means of improved production of hyperpolarized ^{129}Xe , *NMR Biomed.* 13 (4) (2000) 214–219.
- [34] T.A. Kuder, P. Bachert, J. Windschuh, F.B. Laun, Diffusion pore imaging by hyperpolarized Xenon-129 nuclear magnetic resonance, *Phys. Rev. Lett.* 111 (2013) 028101.
- [35] R.H. Acosta, L. Agulles-Pedros, S. Komin, D. Sebastiani, H.W. Spiess, P. Blümler, Diffusion in binary gas mixtures studied by NMR of hyperpolarized gases and molecular dynamics simulations, *Phys. Chem. Chem. Phys.* 8 (2006) 4182–4188.
- [36] K. Demberg, F.B. Laun, J. Windschuh, R. Umatham, P. Bachert, T.A. Kuder, Nuclear magnetic resonance diffusion pore imaging: experimental phase detection by double diffusion encoding, *Phys. Rev. E* 95 (2017) 022404.
- [37] A. Caprihan, L.Z. Wang, E. Fukushima, A multiple-narrow-pulse approximation for restricted diffusion in a time-varying field gradient, *J. Magn. Res. A* 118 (1996) 94–102.
- [38] P.T. Callaghan, A simple matrix formalism for spin echo analysis of restricted diffusion under generalized gradient waveforms, *J. Magn. Reson.* 129 (1997) 74–84.
- [39] A.V. Barzykin, Exact solution of the Torrey-Bloch equation for a spin echo in restricted geometries, *Phys. Rev. B* 58 (1998) 14171–14174.
- [40] D.S. Grebenkov, Laplacian eigenfunctions in NMR. I. A numerical tool, *Conc. Magn. Reson. A* 32A (2008) 277–301.
- [41] D.S. Grebenkov, Pulsed-gradient spin-echo monitoring of restricted diffusion in multilayered structures, *J. Magn. Reson.* 205 (2010) 181–195.
- [42] D.V. Nguyen, J.-R. Li, D. Grebenkov, D. Le Bihan, A finite element method to solve the Bloch-Torrey equation applied to diffusion magnetic resonance imaging, *J. Comput. Phys.* 263 (2014) 283–302.
- [43] P.P. Mitra, P.N. Sen, L.M. Schwartz, P. Le Doussal, Diffusion propagator as a probe of the structure of porous media, *Phys. Rev. Lett.* 68 (1992) 3555–3558.
- [44] P.P. Mitra, P.N. Sen, L.M. Schwartz, Short-time behavior of the diffusion coefficient as a geometrical probe of porous media, *Phys. Rev. B* 47 (1993) 8565–8574.
- [45] N. Moutal, I. Maximov, D.S. Grebenkov, Probing surface-to-volume ratio of an anisotropic medium by diffusion NMR with general gradient encoding, *IEEE Trans. Med. Imag.* (2019), <https://doi.org/10.1109/TMI.2019.2902957>, in press.
- [46] D.S. Novikov, J.H. Jensen, J.A. Helpert, Permeability and surface area of cell membranes from the DWI signal, *Proc. Intl. Soc. Mag. Reson. Med.* 17 (2009) 450.
- [47] P.T. Callaghan, A. Coy, T.P.J. Halpin, D. MacGowan, K.J. Packer, and F.O. Zelaya, Diffusion in porous systems and the influence of pore morphology in pulsed gradient spin-echo nuclear magnetic resonance studies, *J. Chem. Phys.* 97 (1992) 651–662.
- [48] P.T. Callaghan, Pulsed-gradient spin-echo NMR for planar, cylindrical, and spherical pores under conditions of wall relaxation, *J. Magn. Reson. A* 113 (1995) 53–59.
- [49] P. Linse, O. Söderman, The validity of the short-gradient-pulse approximation in NMR studies of restricted diffusion. Simulations of molecules diffusing between planes, in cylinders, and spheres, *J. Magn. Reson. A* 116 (1995) 77–86.
- [50] B. Robertson, Spin-echo decay of spins diffusing in a bounded region, *Phys. Rev.* 151 (1966) 273–277.
- [51] D.S. Novikov, E. Fieremans, J.H. Jensen, J.A. Helpert, Random walks with barriers, *Nat. Phys.* 7 (2011) 508–514.
- [52] D.S. Novikov, J.H. Jensen, J.A. Helpert, E. Fieremans, Revealing mesoscopic structural universality with diffusion, *PNAS* 111 (2014) 5088–5093.
- [53] P. Le Doussal, P.N. Sen, Decay of nuclear magnetization by diffusion in a parabolic magnetic field: an exactly solvable model, *Phys. Rev. B* 46 (1992) 3465–3485.